In situ investigation of the CO$_2$ methanation on carbon/ceria-supported Ni catalysts using modulation-excitation DRIFTS

Liliana P.L. Gonçalves [a,b,c], Jerrik Mielby [d], O. Salomé G.P. Soares [b,c], Juliana P.S. Sousa [a], Dmitri Y. Petrovykh [a], Oleg I. Lebedev [e], M. Fernando R. Pereira [b,c,*], Søren Kegnæs [d,**], Yury V. Kolen'ko [a,**]

[a] *International Iberian Nanotechnology Laboratory, 4715-330 Braga, Portugal*
[b] *Laboratory of Separation and Reaction Engineering – Laboratory of Catalysis and Materials (LSRE–LCM), Faculty of Engineering, University of Porto, 4200-465 Porto, Portugal*
[c] *ALiCE - Associate Laboratory in Chemical Engineering, Faculty of Engineering, University of Porto, Rua Dr. Roberto Frias, 4200-465 Porto, Portugal*
[d] *DTU Chemistry, Technical University of Denmark, Kemitorvet 207, 2800 Kongens Lyngby, Denmark*
[e] *Laboratoire CRISMAT, UMR 6508, CNRS–ENSICAEN, Caen 14050, France*

ARTICLE INFO

ABSTRACT

The development of novel cost-efficient, high-performing catalysts for CO$_2$ methanation that are active at low temperatures can be optimized through the understanding of the reaction mechanism on different materials. A series of Ni-based catalysts supported on CeO$_2$ and carbon/CeO$_2$ composites was investigated, showing that Ni nanoparticles supported on a carbon/CeO$_2$ composite with a 50:50 wt ratio and on pure CeO$_2$ have excellent low-temperature activity and achieve up to 87% CO$_2$ conversion with full selectivity towards CH$_4$ at 370 °C. Importantly, meaningful insights on the reaction mechanism were gathered for the different types of materials by using the emerging ME−PSD−DRIFTS technique. The study of the rate of formation/consumption of the various intermediates showed that the CO$_2$ methanation reaction follows a combination of the CO and formate pathways in the case of Ni on pure CeO$_2$; however, in the case of Ni on the carbon/CeO$_2$ composite, it follows only the formate pathway.

1. Introduction

The CO$_2$ methanation reaction (CO$_2$ + 4 H$_2$ → CH$_4$ + 2 H$_2$O, $\Delta H_{298\,K}$ = −165 kJ mol^{-1}) is the most thermodynamically favorable reaction of CO$_2$ hydrogenation, and is a promising way to convert anthropogenic CO$_2$ back to CH$_4$ fuel [1–4]. The hydrogenation proceeds through an eight-electron reduction process with consequent significant kinetic barriers, thus requiring the action of a catalyst. From the mechanistic perspective, extensive research has been conducted on CO$_2$ methanation. Nevertheless, the reaction mechanism is still vigorously debated, since it depends on the catalytic material and the hydrogenation conditions [1,3]. The most predominant mechanisms proposed in the literature can be grouped in two different categories: (i) the dissociative pathway, where CO$_2$ is dissociated into CO, which acts as the main intermediate, and (ii) the associative pathway, where CO$_2$ is molecularly adsorbed associatively with a H atom previously adsorbed on the surface, forming formate as an intermediate, i.e., without CO formation [3].

CO$_2$ methanation has played a significant role in understanding CO$_2$ hydrogenation and the associated development of catalysts. Importantly, researchers continue to exploit different catalysts to achieve high CO$_2$ conversion and complete selectivity towards CH$_4$. For example, a number of catalysts based on transition metals (Ni, Co, Fe) or platinum-group metals (Ru, Rh) dispersed on porous supporting materials have been developed [2,5–12]. Notably, Ni-based catalysts, compared to platinum-group metals, exhibit an optimal combination of activity, selectivity, and low price [2,5,6]. Despite the advances in using Ni catalysts for CO$_2$ methanation, a way to reduce the reaction temperature from the current ≥ 400 °C while preserving high catalytic performance remains a challenge.

One interesting approach to address this challenge is to develop Ni

---

catalysts supported on novel materials. Traditionally, alumina (Al_2O_3) is used as supporting material for Ni methanation catalysts [13–15]. In contrast, we and other researchers have focused on carbon supporting materials [2,5,16,17]. An exciting feature of these high-surface-area porous supports are their versatile surface properties [18]. Specifically, via modification of their surface chemistry, carbon materials can exhibit increased basicity, which improves the CO_2 coverage of the catalyst, since it is an acidic molecule, thus enhancing the CO_2 methanation performance at lower reaction temperatures [2]. Compared to the more common Ni supported on metal oxides, the research on Ni supported on carbon materials is less advanced, motivating a fundamental investigation of such alternative catalytic systems [2,5].

Among the metal-oxide supporting materials, despite being based on a rare-earth metal, ceria (CeO_2) has emerged as a promising alternative to Al_2O_3 because it enhances the metal–support interactions, leading to high dispersion of the resultant Ni nanoparticles over the support. Moreover, owing to the enhanced surface coverage by CO_2 species, enabled by the CeO_2 surface basicity, it improves the low-temperature catalytic performance of the catalysts in CO_2 methanation [19–26]. These positive effects of CeO_2 motivated us to develop high-performing carbon/ceria-supported Ni catalysts for CO_2 methanation, as well as to conduct a comparative mechanistic study of CO_2 hydrogenation over these catalysts.

In this work, we report the successful precipitation synthesis of a composite supporting material consisting of reduced activated carbon (ACR) and CeO_2 (ACR–CeO_2) as well as pure CeO_2, followed by deposition of Ni nanoparticles via the incipient wetness impregnation route. An important feature of our findings is the remarkable reduction by 80 °C of the optimal temperature of the CO_2 methanation reaction, compared to that for a CeO_2-free Ni/ACR catalyst developed in our previous study [2], thus significantly improving the sustainability of the methanation approach without jeopardizing the catalytic performance. Furthermore, we conducted a detailed *in situ* modulation-excitation phase-sensitive-detection diffuse-reflectance infrared Fourier-transform spectroscopy (ME–PSD–DRIFTS) investigation of the methanation over the newly synthesized high-performing Ni/ACR–CeO_2 and Ni/CeO_2 catalysts, to obtain key mechanistic insights.

2. Experimental methods

2.1. Synthesis

In the present work, we synthesized reduced activated carbon (ACR) with Lewis base sites by heat-treatment of a commercial NORIT GAC 1240 PLUS activated carbon (CABOT) at 900 °C for 1 h under H_2 flow [2]. Pure CeO_2 and composite ACR–CeO_2 supporting materials were prepared by a precipitation method adapted from elsewhere [27]. Briefly, $Ce(NO_3)_3 \cdot 6H_2O$ is precipitated by NaOH under vigorous stirring, along with the addition of calculated amounts of ACR for the composite ACR–CeO_2 synthesis. The 15% Ni nanoparticles were deposited onto as-synthesized supporting materials via incipient wetness impregnation using $Ni(NO_3)_3 \cdot 6H_2O$, followed by heat treatment to decompose nitrate, thus generating metallic Ni (**Ni/CeO_2** and **Ni/ACR$-$$CeO_2$**).

2.2. Characterization

The synthesized materials were characterized by N_2 physisorption, powder X-ray diffraction (XRD), H_2 temperature programmed reduction (H_2–TPR), H_2–chemisorption, X-ray photoelectron spectroscopy (XPS), transmission electron microscopy (TEM), energy-dispersive X-ray spectroscopy in scanning TEM mode (STEM–EDX).

2.3. Catalytic testing

The activity, selectivity, and stability of the synthesized catalysts in CO_2 methanation were evaluated in a Microactivity XS15 system (PID

Eng & Tech), using a fixed bed quartz reactor ($\emptyset_{int}$ = 1 cm). Outflow products were analyzed online using a GC 1000 gas chromatograph (DANI), equipped with a thermal conductivity detector (TCD) and a GS-CarbonPLOT capillary column, while using He as the carrier gas and a continuous flow of N_2 as the internal standard. Each catalyst (100 mg) was diluted by inert SiC material, and then was pre-treated in situ under H_2 flow (40 $cm^3 \, min^{-1}$) at its reduction temperature for 30 min, at 1 bar. After that, the reactor temperature was decreased to 100 °C under He (50 $cm^3 \, min^{-1}$), and then, the reactor was fed with 10% CO_2, 40% H_2 (the stoichiometric composition) and 50% He, with a total flowrate of 100 $cm^3 \, min^{-1}$. A temperature ramping from 100 to 500 °C at a rate of 5 °C min^{-1} was performed under reaction conditions to evaluate the catalytic properties of the catalysts at various temperatures. Additionally, isothermal time-on-stream (TOS) experiments were conducted under the same reaction conditions to evaluate the stability of the catalysts.

2.4. In situ spectroscopy

CO_2 adsorption and CO_2 methanation over the synthesized materials were probed using steady-state *in situ* diffuse reflectance infrared Fourier transform spectroscopy (DRIFTS) using a Nicolet iS50 FTIR spectrometer (Thermo Scientific), equipped with a Mercury-Cadmium-Telluride (MCT) detector and a high temperature reaction chamber (Harrick Scientific). Additionally, the CO_2 methanation over the prepared materials was investigated by *in situ* modulation excitation phase-sensitive detection DRIFTS (ME–PSD–DRIFTS) using the same spectrometer. The ME-PSD analysis highlight the species that change with the modulation frequency (f). The collected spectra were converted into the so-called frequency domain by Fast Fourier Transform (FFT). The data was then filtered at the modulation frequency and converted into the phase-domain by Inverse Fast Fourier Transform (IFFT). Activated carbon absorbs most of the IR radiation, so it was not possible to perform DRIFTS analyses in the Ni/ACR sample.

Readers interested in the detailed experimental information are referred to the Supplementary material (SM).

3. Results

3.1. CO_2 methanation over Ni/CeO_2 and Ni/ACR–CeO_2

In our previous study [2], a novel methanation catalyst with 15 wt% Ni loading over ACR having O-free Lewis basic sites (denoted as **Ni/ACR**) has been developed, exhibiting CO_2 conversion (X_{CO2}) of 76% and selectivity towards CH_4 (S_{CH4}) of 97%, but at a fairly high reaction temperature of 450 °C. To increase the conversion while lowering the reaction temperature, we sought to introduce CeO_2, thus forming a composite supporting material with ACR. We began by optimizing the CeO_2 loading in the ACR–CeO_2 composite support. It was established that 15 wt% Ni catalyst supported on ACR–CeO_2 with ACR:CeO_2 weight ratio of 50:50 exhibits the optimal catalytic properties in CO_2 methanation (Fig. S1). Hence, we further conducted our studies with this catalyst, hereafter referred to as **Ni/ACR–CeO_2**.

With the optimized composite catalyst in hand, we investigated its methanation performance and compared it to a control 15 wt% Ni catalyst supported on pure CeO_2 (denoted as **Ni/CeO_2**).

Fig. 1a,b show the obtained X_{CO2} and S_{CH4} results in the temperature range of 200–500 °C. Both catalysts start to convert CO_2 from ca. 200 °C reaching X_{CO2} = 50% at 280 °C, the so-called T_{50}.

Upon the temperature increase, the catalysts further achieve CO_2 conversions that are very close to the thermodynamic equilibrium, exhibiting maximum X_{CO2} of 85.7% (**Ni/CeO_2**) and 87.4% (**Ni/ACR–CeO_2**) at a notably low temperature of only 370 °C (Fig. 1a). In terms of S_{CH4}, the catalysts also demonstrate values comparable to the thermodynamic equilibrium over the range of the studied temperatures, with $S_{CH4} \approx 100\%$ at maximum X_{CO2} (Fig. 1a,b), with the only
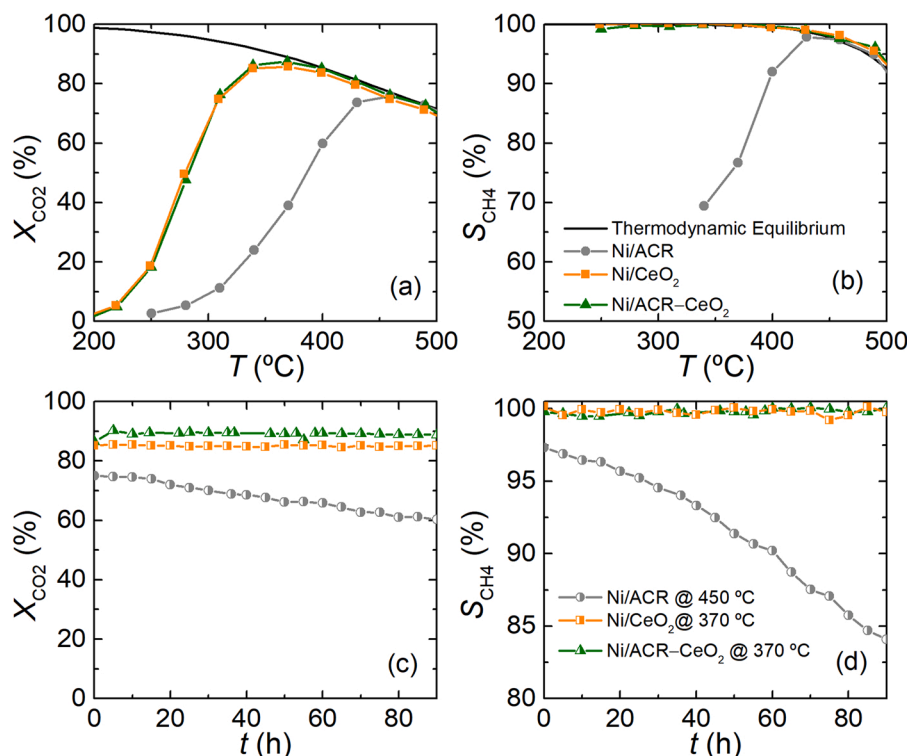
Fig. 1. Comparison of X_{CO2} (a) and S_{CH4} (b) as a function of reaction temperature, together with the stability testing results in terms of X_{CO2} (c) and S_{CH4} (d) over 90 h TOS of the new Ni/CeO$_2$ and Ni/ACR–CeO$_2$ catalysts in comparison with previously reported ceria-free Ni/ACR [2]. The thermodynamic equilibrium curves were calculated using a model based on the minimization of Gibbs free-energy of the existing species. Methanation conditions: $P = 1$ bar; $WHSV = 60$ 000 cm^3 g^{-1} h^{-1}; CO$_2$: H$_2$ (V:V) = 1: 4.

byproduct being CO. We finally investigated the stability of the catalysts through a long time-on-stream (TOS) testing at the best performing temperature of 370 °C. It was established that both the control **Ni/CeO$_2$** and composite **Ni/ACR−CeO$_2$** demonstrate excellent stability over 90 h on stream with no loss in either X_{CO2} or S_{CH4} (Fig. 1c,d). Importantly, a comparison of the catalytic properties between the new carbon/ceria-containing **Ni/ACR–CeO$_2$** and our previously reported carbon-containing **Ni/ACR** [2] (Fig. 1) evidently highlights that the compositing of ACR with CeO$_2$ not only leads to a significant improvement in the methanation performance but also simultaneously lowers the optimal reaction temperature by 80 °C (from 450 °C for **Ni/ACR** to 370 °C for **Ni/ACR–CeO$_2$**). Moreover, the compositing of ACR with CeO$_2$ leads to an improvement in stability at the respective optimal temperature of the resultant **Ni/ACR–CeO$_2$** catalyst, relative to that of **Ni/ACR** [2] (Fig. 1).

3.2. Characterization of the catalysts

Our catalytic testing reveals that both **Ni/CeO$_2$** and **Ni/ACR–CeO$_2$** exhibit similarly excellent catalytic properties at reasonably low reaction temperatures, despite being based on different supporting materials. Therefore, we characterized the catalysts to determine the parameters that govern the methanation performance.

Even though **Ni/CeO$_2$** and **Ni/ACR–CeO$_2$** have similar catalytic properties (Fig. 1), the data presented in Table 1 demonstrate that the catalysts exhibit quite different textural properties. The textural properties of the synthesized materials were estimated using Brunauer–Emmett–Teller (BET) and Barrett–Joyner–Halenda (BJH) methods. Pure CeO$_2$ support has a relatively low specific surface area (S_{BET}) of 104 m^2 g^{-1}, while the pure ACR support has about 7-fold higher S$_{BET}$ = 784 m^2 g^{-1}. As expected, the composite ACR–CeO$_2$ exhibits a S_{BET} = 373 m^2 g^{-1} that is higher than that of pure CeO$_2$, but lower than that of pure ACR. This trend is sustained for the respective Ni catalysts supported on the two materials, exhibiting a decreasing order in S_{BET} **Ni/ACR–CeO$_2$** > **Ni/CeO$_2$** (Table 1). The addition of Ni leads to a slight decrease in S_{BET} compared to the respective supporting materials (Table 1). Both CeO$_2$ and ACR–CeO$_2$ supports, and the derivative catalysts present Type IV isotherms (Fig. S2); the pore-size-distribution data (Fig. S3) reveal that **Ni/CeO$_2$** exhibits a higher number of pores having larger width, while **Ni/ACR−CeO$_2$** has a peak in the smaller width range, also containing pores with diameters higher than 5 nm.

Next, we probed the metal–support interactions and metallic surface areas of **Ni/CeO$_2$** and **Ni/ACR–CeO$_2$**. The comparison of hydrogen temperature-programmed reduction (H$_2$–TPR) profiles of **Ni/CeO$_2$** and

Table 1

Textural properties [specific surface area (S_{BET}), and total pore volume (V_p)], average size of CeO$_2$ crystallites ($d_{c,CeO2}$), and Ni crystallites ($d_{c,Ni}$), metallic Ni surface area (S_M), temperature at which $X_{CO2} = 50\%$ (T_{50}), and maximum X_{CO2}, attained at 450 °C for Ni/ACR [2] and 370 °C for Ni/CeO$_2$ and Ni/ACR–CeO$_2$.

	S_{BET} (m^2 g^{-1})[a]	V_P (cm^3 g^{-1})[a]	$d_{c,Ni}$ (nm)[b]	$d_{c,CeO2}$ (nm)[b]	S_M (m^2 g$_{cat}^{-1}$)[c]	T_{50} (°C)	Max X_{CO2} (%)
ACR [2]	784	0.48	–	–	–	–	0
CeO$_2$	104	0.17	–	7	–	–	12
ACR–CeO$_2$	373	0.33	–	6	–	–	11
Ni/ACR [2]	656	0.41	8	–	2.73	385	76
Ni/CeO$_2$	82	0.14	9	7	1.66	280	86
Ni/ACR–CeO$_2$	386	0.30	5	5	2.57	280	87

[a] Estimated by N$_2$ physisorption.
[b] Estimated from XRD data using Scherrer equation.
[c] Estimated by H$_2$ pulse chemisorption.

Ni/ACR–CeO₂ demonstrate different metal–support interactions between Ni nanoparticles and the supporting materials (Fig. S4a). Specifically, **Ni/CeO₂** exhibits a large peak at 360 °C with a shoulder at 404 °C, as well as two small shoulders at 334 °C and 464 °C. In contrast, **Ni/ACR–CeO₂** exhibits a large peak at a lower temperature of 320 °C with two high-temperature shoulders at 392 °C and 502 °C. Apparently, **Ni/CeO₂** is largely composed of Ni species that exhibit a stronger interaction with pure CeO₂ support, compared to that in composite **Ni/ACR–CeO₂**. Regarding the Ni surface area (S_M), measured using H₂ pulse chemisorption, it was estimated that **Ni/ACR–CeO₂** exhibits more than 1.5 times higher metallic Ni surface than does **Ni/CeO₂** (Table 1). The H₂–TPR of the supporting materials was also assessed (Fig. S4b) and it was observed that the H₂ consumed for CeO₂ reduction is minimal when comparing to the H₂ consumed for the reduction of the Ni-based catalysts. Additionally, the analysis of the H₂−TPR profiles indicate that the ACR−CeO₂ support is a homogeneous mixture that interacts in a way that the reduction profile of the **Ni/ACR−CeO₂** sample is different than that of the other two supports (CeO₂ and ACR), and not a combination of both **Ni/CeO₂** and **Ni/ACR** [2] H₂-TPR profiles.

To gain structural insight into the synthesized materials, we further investigated their phase composition using powder X-ray diffraction (XRD). According to the XRD patterns (Fig. S5), the as-synthesized pure and composite supports contain cubic CeO₂ phase (ICDD #04–006–1932). In contrast, the respective Ni catalysts additionally contain cubic metallic Ni (ICDD #04–016–4761), with no secondary phases being present. There is possibly a graphitic carbon peak, but since it should be present at 28°, overlapping with a peak from CeO₂, it is impossible to access its presence. The average size of Ni and CeO₂ crystallites was assessed from XRD data using the Scherrer equation (Table 1), and the size of Ni crystallites in **Ni/CeO₂** (ca. 9 nm) was estimated to be nearly 2 times larger than in **Ni/ACR–CeO₂** (ca. 5 nm), which is consistent with the smaller S_M of **Ni/CeO₂**.

X-ray photoelectron spectroscopy (XPS) analysis revealed that both catalysts, **Ni/CeO₂** and **Ni/ACR–CeO₂**, exhibited two different Ni phases, observed from the deconvolution of the XPS data for Ni 2p₃/₂ (Fig. 2). The lower energy component (853.0 ± 0.1 eV) is assigned to Ni⁰ in metallic Ni species, while the components at 854.4 ± 0.2 eV and 856.4 ± 0.1 eV are consistent with Ni²⁺ in nickel-oxide phase, and the ones at 861.3 ± 0.3 eV and 864.3 ± 0.1 eV are satellite peaks from Ni²⁺. The Ni 2p₃/₂ spectral envelopes of the catalysts resemble the typical spectra for nanoscale oxidation layers on Ni and Ni compounds, being consistent with a thin, predominantly Ni²⁺, nickel oxide layer on metallic Ni [5,28–30]. The binding energies (BEs) of fitting components are presented in Table S1 and the relative atomic percentages (at%) of Ni⁰ and Ni²⁺ are presented in Table S2. The relative atomic percentage

of Ni⁰ is similar in **Ni/ACR–CeO₂** and **Ni/CeO₂** catalysts, at 4.2 at% and 4.4 at%, respectively (Table S2).

The Ce 3d spectra also revealed the presence of mixed Ce phases (Fig. 2) in both samples. The spectra can be represented as five pairs of doublets, identified in Fig. 2 as u and v for the Ce 3d₃/₂ and Ce 3d₅/₂ spin–orbit components, with spin–orbit splitting of 18.4 ± 0.5 eV for all the samples, consistent with those found in the literature [31,32]. These spectra were fitted using a method similar to that reported by Zhang et al. [32] where the u''' peak is fixed and the remaining peaks are constrained according to the u''' position.

The v⁰, u⁰, v', and u' are attributed to Ce³⁺, while the highest biding energy peaks, v''' and u''', are attributed to the primary components of Ce⁴⁺, and the remaining v, u, v'', and u'', are identified as "shake-down" states, as reported by Mullins et al. [31,33] Table S2 presents the BEs of each of these components. Importantly, we note that there is a small overlap of the Ni 2p₁/₂ components (orange lines and symbols below 881 eV in Fig. 2) and the low-BE components in the Ce 3d spectra. This overlap was accounted for by including in the Ce 3d fitting procedure Ni 2p₁/₂ components (orange lines in Fig. 2), with fixed parameters based on the more reliable fits in the Ni 2p₃/₂ region.

The Ce 3d peaks in **Ni/ACR–CeO₂** are noticeably narrower than those in **Ni/CeO₂**, which likely indicates that ceria nanoparticles are in a more uniform electrostatic environment in **Ni/ACR–CeO₂**, where they are in a good electrical contact with the carbon substrate.

The amount of Ce⁴⁺ and reduced Ce³⁺ is quantified in Table S2. Interestingly, the **Ni/ACR–CeO₂** catalyst exhibits a higher relative at% of Ce³⁺ (20.5 at%) compared to **Ni/ACR–CeO₂** that contains 16.4 at% Ce³⁺.

The C 1s spectra of **Ni/ACR–CeO₂** were also analyzed, and the results are presented in Fig. S6 [35,36].

Interested in understanding the microstructural properties of the catalysts, we then conducted transmission electron microscopy (TEM) and energy-dispersive X-ray spectroscopy in scanning STEM mode (STEM–EDX) analyses. These studies reveal metallic Ni nanoparticles well-dispersed over nanocrystalline CeO₂ and amorphous-like ACR. Fig. 3a shows TEM image of Ni nanoparticles in **Ni/CeO₂**, where it is possible to distinguish only some large Ni particles (ca. 30–50 nm) dispersed over CeO₂ support. Fig. 3e shows Ni nanoparticles dispersed on composite ACR–CeO₂ support in **Ni/ACR–CeO₂**, wherein the Ni particles (ca. 5–10 nm) dispersed on ACR and some larger Ni particles (ca. 30–50 nm) on CeO₂ are observed. It is important to note that the imaging contrast between the Ni and CeO₂ nanoparticles is very low, thus it is difficult to differentiate the two types of nanoparticles in the electron microscopy images. Therefore, the size ranges indicated are merely representative of the observed identifiable nanoparticles, leading
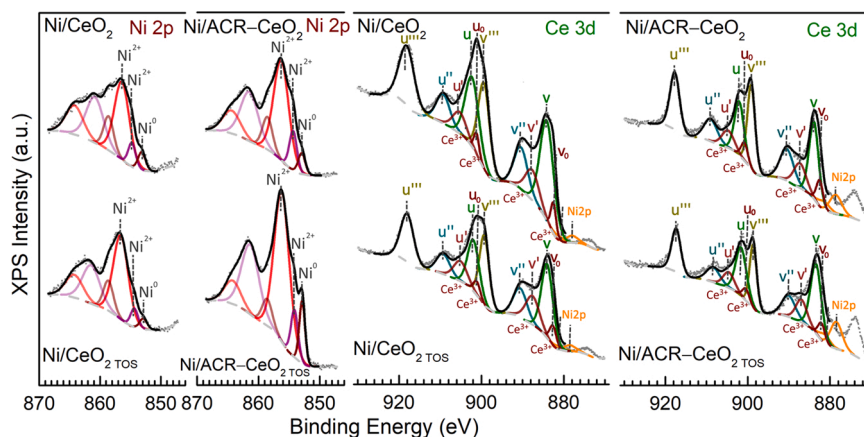

Fig. 2. High-resolution XPS data for the Ni 2p₃/₂ and Ce 3d region collected from as-synthesized and TOS-tested Ni/CeO₂ and Ni/ACR−CeO₂. Symbols: raw data; black lines: overall fits; colored lines: fits of individual components; dashed lines: background. The observed binding energies (BE) and assignment of the peak positions are summarized in Table S1.
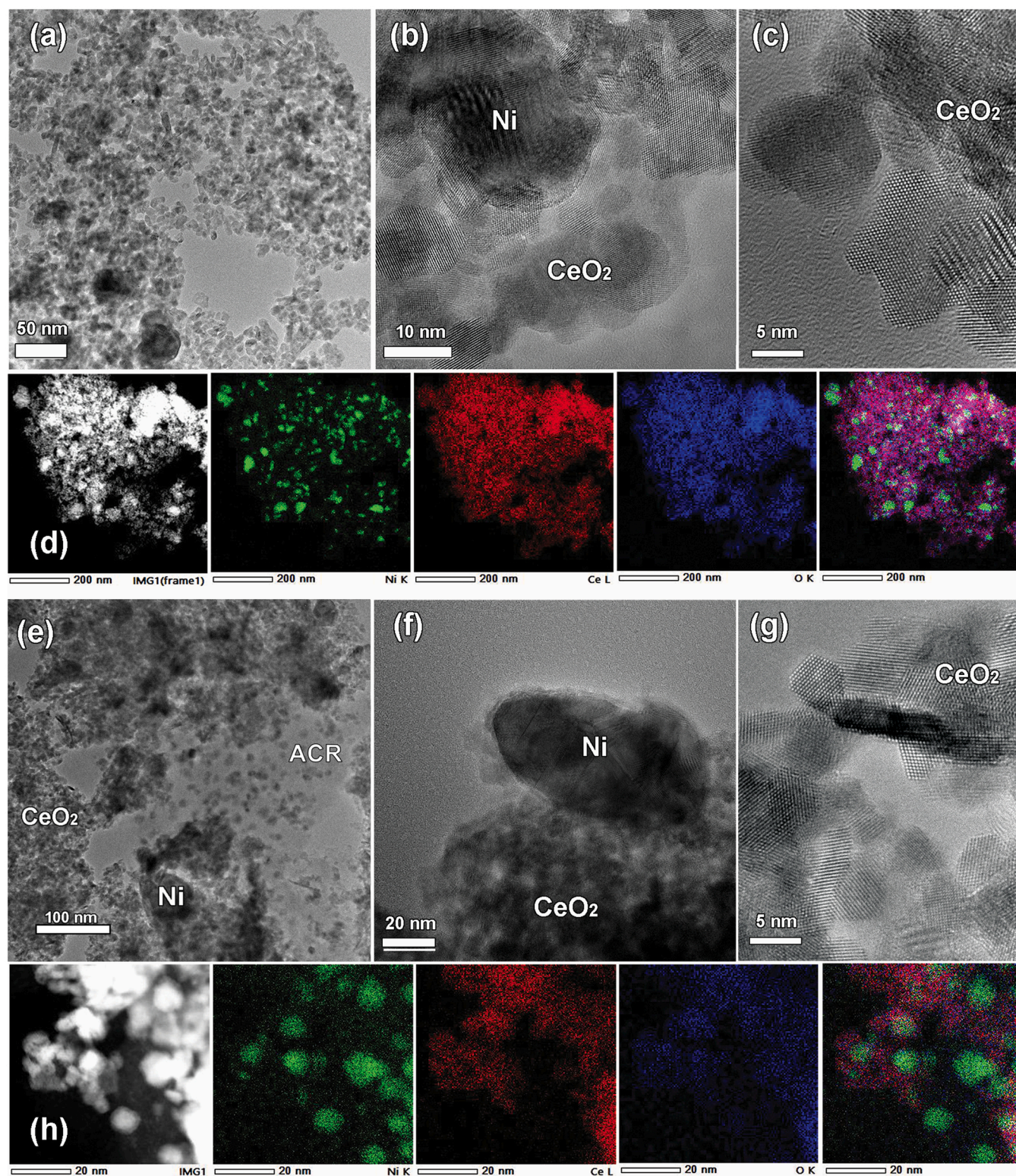
Fig. 3. TEM images of Ni nanoparticles dispersed on CeO_2 (a) and $ACR–CeO_2$ (e) supporting materials, together with the representative HRTEM images of Ni and CeO_2 nanoparticles in the Ni/CeO_2 (b,c) and $Ni/ACR–CeO_2$ (f,g) catalysts. Low-magnification STEM images of the Ni/CeO_2 (d) and $Ni/ACR–CeO_2$ (h) catalysts, together with the respective STEM–EDX maps for Ni, Ce, O and their mixture.

to a gap between the Ni nanoparticles sizes from TEM and those estimated by XRD, which is more representative.

Although it is difficult to distinguish the smaller Ni particles on the CeO_2 support due to the low contrast on the TEM images, the respective STEM–EDX maps evidence that there are also small Ni particles dispersed on CeO_2 material in both **Ni/CeO_2** and **Ni/ACR–CeO_2** catalysts (Fig. 3d,h). A closer look at CeO_2 supporting material in **Ni/CeO_2** (Fig. 3c) and **Ni/ACR–CeO_2** (Fig. 3g) catalysts reveals that the ceria consists of agglomerated CeO_2 nanoparticles (ca. 5–10 nm), preferentially faceted by the {110} plane.

Interestingly, high-resolution TEM (HRTEM) imaging of Ni nanoparticles in **Ni/CeO₂** and **Ni/ACR-CeO₂** reveals that the particles in both catalysts exhibit Ni@NiO core-shell appearance. As an example, Fig. 4a,b show HRTEM images of a Ni nanoparticle in **Ni/ACR-CeO₂** catalyst, together with the corresponding Fourier transform (FT) patterns for the Ni core and NiO shell. Furthermore, multiple twinning of the Ni nanoparticle can be observed in the HRTEM images, marked by white arrow heads.

Even though there was no loss in X_{CO2} and S_{CH4} over 90 h of TOS testing (Fig. 1c,d), we decided to investigate the impact of the reaction conditions on the microstructure and chemical composition of the catalysts by means of electron microscopy and XPS.

The Ni $2p_{3/2}$ spectra (Fig. 2) of the samples after TOS testing (**Ni/CeO₂ ₜₒₛ** and **Ni/ACR-CeO₂ ₜₒₛ**) include fitting components at BEs similar to those of the components in the spectra of fresh **Ni/CeO₂** and **Ni/ACR-CeO₂** catalysts. Considering the relative Ni⁰ atomic content (Table S2), however, we observed that it decreases to 2.8 at% (cf. 4.4%) in the case of **Ni/CeO₂ ₜₒₛ** and, on the contrary, increases to 7.4 at% (cf. 4.2 at%) in the case of **Ni/ACR-CeO₂ ₜₒₛ**. In the Ce 3d spectra (Fig. 2), again the positions of the peaks remain similar for both catalysts after 90 h of TOS, but there are differences in the Ce^{3+}/Ce^{4+} ratio before and after TOS in both **Ni/CeO₂** and **Ni/ACR-CeO₂**. The Ce^{3+} atomic content in **Ni/CeO₂** increases to 21.3 at% (cf. 16.4 at%), while in **Ni/ACR-CeO₂**, it remains approximately constant with 19.9 at% (cf. 20.5 at%).

From Figs. S8a-d, one can see that the TOS-tested **Ni/CeO₂** maintains the microstructure of the Ni nanoparticles dispersed over the ceria support composed by small CeO₂ nanoparticles (ca. 5–10 nm), similar to that in pristine **Ni/CeO₂** (Fig. 3a). In contrast, TOS-tested **Ni/ACR-CeO₂** undergoes significant microstructural changes within CeO₂ support. Specifically, Fig. S8e evidences the appearance of CeO₂ particles with a needle-like shape after 90 h of methanation. Such nanoneedles were not observed in pristine **Ni/ACR-CeO₂** (Fig. 3e) or pristine and TOS-tested **Ni/CeO₂** (Fig. 3a, S8a).

Notably, a closer look at Ni particles in TOS-tested **Ni/CeO₂** (Fig. S8c) and **Ni/ACR-CeO₂** (Fig. 4c,d) indicates a preservation of Ni@NiO core-shell nanostructure of the catalyst after prolonged methanation.

3.3. Probing the mechanism of CO₂ methanation by in situ DRIFTS

Having in hand two well-characterized high-performing methanation catalysts, we further conducted *in situ* DRIFTS studies to elucidate the reaction mechanism over **Ni/CeO₂** and **Ni/ACR-CeO₂**. This technique is used to understand the reaction mechanism in heterogeneous catalysis, probing the adsorbed species on the catalysts under reaction conditions. There are some drawbacks of this technique. Specifically, it detects not only the intermediate species but also the sample background, noise, and spectator species, making it difficult to distinguish what are the real intermediates of the reaction [37,38].

Furthermore, the intermediate species have a short lifetime, making it even more difficult to differentiate them from the remaining species, which are present under steady-state conditions. Fortunately, the modulation-excitation (ME) technique offers an interesting solution for overcoming the aforementioned drawbacks. It is based on the introduction of a rapid periodic perturbation on the testing system, to which only the intermediate species of the reaction respond. The resultant spectroscopic signal is then analyzed by phase-sensitive detection (PSD) technique to enhance the signal-to-noise ratio and to extract the information about intermediate species that responded to the modulation signal, thus avoiding the signal from the spectator species [10,37–41].

We started by performing steady-state *in situ* DRIFTS for CO₂ adsorption and then for CO₂ methanation at 250, 300, and 350 °C. In this temperature range, the X_{CO2} goes from low to almost complete. Fig. S9 shows the full range spectra for each experiment, along with a discussion of the observed trends for hydroxyl groups, gaseous CO₂, and gaseous CH₄ [42]. Fig. 5 displays a zoom-in of the region below 2000 cm⁻¹, which carries important information about the CO₂ adsorption and methanation mechanisms, while Table 2 summarizes the respective band assignment. During CO₂ adsorption (Fig. 5a,c), two bands detected at 1500 and 1370 cm⁻¹ (ν_{as} / ν_s) can be attributed to formate (HCOO) species, which are probably close to a reduced Ce site in CeO₂, because they have a low $\Delta_{as-s} = 130 / 150$ cm⁻¹ [10,26]. Two other bands are observed at 1600 and 1280 cm⁻¹ (ν_{as} / ν_s), that can be assigned to bi-dentate carbonates (b–CO₃), along with the band at 1030 cm⁻¹ [10,26]. Moreover, a small band at 1415 cm⁻¹ is also observed in the spectrum of **Ni/CeO₂** at 250 °C, which can be attributed
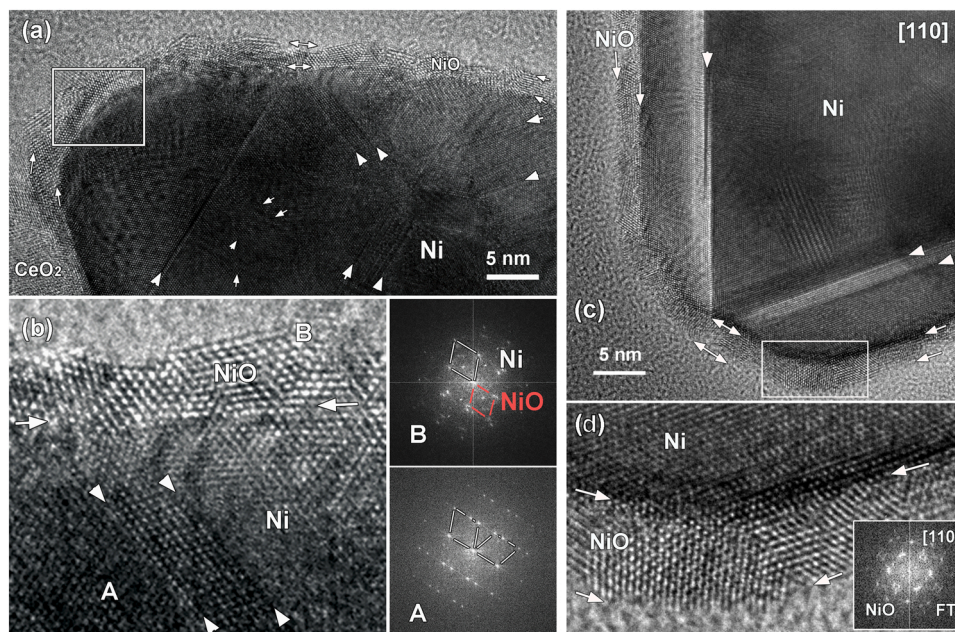

Fig. 4. HRTEM imaging of the surface of a single Ni nanoparticle in the as-synthesized Ni/ACR–CeO₂ catalyst (a) and zoom-in (white rectangle) image (b) and in the same catalyst after its TOS testing for 90 h (c,d), revealing the core-shell appearance of the nanoparticles. The insets in (b,d) show the FT patterns from the corresponding regions. The white arrows mark the NiO shell and the white arrow heads depict the twinning within the Ni nanoparticles.
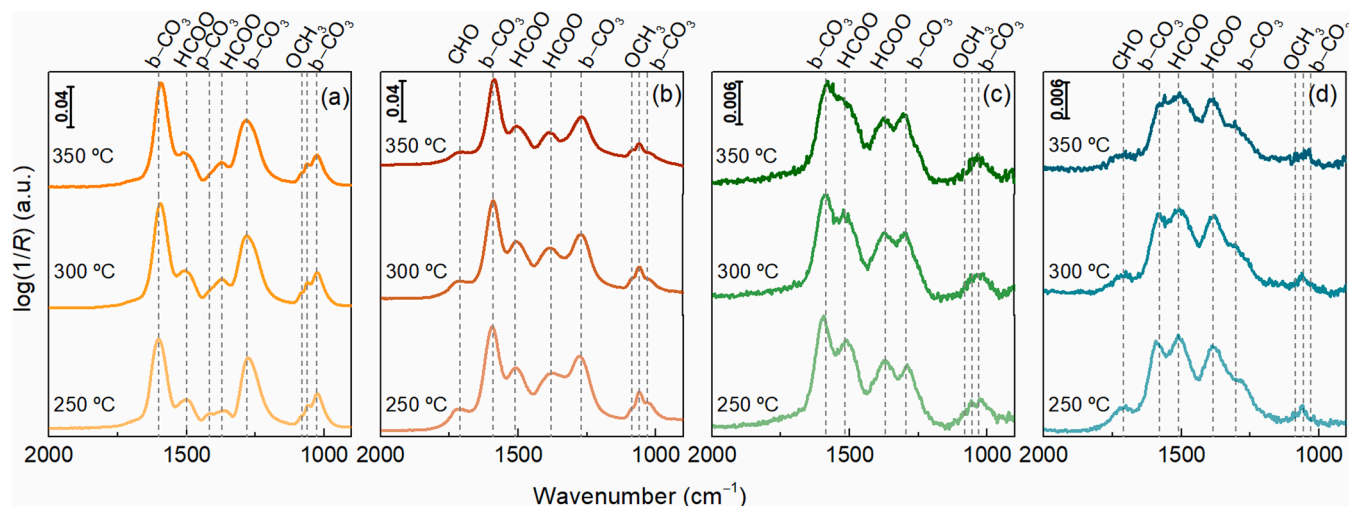
Fig. 5. Steady-state *in situ* DRIFTS studies of CO_2 adsorption and methanation over Ni/CeO_2 (a,b) and $Ni/ACR–CeO_2$ (c,d) catalysts. Experimental conditions for CO_2 adsorption: $P = 1$ bar; CO_2 flowrate of 2.5 cm³ min⁻¹; N_2 flowrate of 100 cm³ min⁻¹; $m_{cat} = 15$ mg. Experimental conditions of CO_2 methanation: $P = 1$ bar; CO_2 flowrate of 2.5 cm³ min⁻¹; 10%H_2/N_2 gas mixture flowrate of 100 cm³ min⁻¹; $m_{cat} = 15$ mg. The dashed lines indicate the positions of the observed peaks.

Table 2
Assignment of the bands observed during steady-state DRIFTS and ME–PSD–DRIFTS experiments: hydroxyl groups (OH^-), gaseous methane (CH_4), gaseous carbon dioxide (CO_2), bridged carbon monoxide (br–CO), formyl groups (CHO), bi-dentate carbonates (b–CO_3), poly-dentate carbonates (p – CO_3), formates (HCOO), carboxylate ($CO_2^{-\delta}$), and methoxy groups (OCH_3).

	Steady-state *in situ* DRIFTS				*In situ* ME−PSD−DRIFTS	
	CO₂ adsorption		CO₂ methanation		CO₂ adsorption	
	Ni/CeO₂	Ni/ACR−CeO₂	Ni/CeO₂	Ni/ACR−CeO₂	Ni/CeO₂	Ni/ACR−CeO₂
	Wavenumber (cm⁻¹)					
CO₂/ OH⁻	3750 − 3550	3750 − 3550	3750 − 3550	3750 − 3550	3750 − 3550	3750 − 3550
CH₄	−	−	−	3017	3017	3017
CO₂	2400 − 2250	2400 − 2250	2400 − 2250	2400 − 2250	2400 − 2250	2400 − 2250
CO gas	−	−	−	2200 − 2100	2200 − 2100	2200 − 2100
br−CO	−	−	−	−	1760	1770
CHO	−	−	1710	1710	1700	1700
b−CO₃	1600	1585	1590	1580	1610	1600
	1280	1295	1270	1300	1290	1290
	1030	1030	1030	1030	1020	1020
p − CO₃	1415	−	−	−	1450	1450
	−	−	−	−	1405	1405
HCOO	1500	1520	1510	1510	1520	1530
	1370	1370	1380	1385	1360	1360
CO₂⁻δ	−	−	−	−	1240	1240
OCH₃	1080	1080	1080	1080	1080	1080
	1060	1060	1060	1060	1060	1060

to poly-dentate (p–CO_3) carbonates Interestingly, a small amount of methoxy species (OCH_3) are present in the CO_2 adsorption spectra without H_2 being present, corresponding to the bands at 1080–1060 cm⁻¹ [24,25]; therefore, residual H_2 should be present on the Ni nanoparticles from the reduction pre-treatment which might lead to the methoxy formation during CO_2 adsorption step.

When H_2 is introduced into the gas flow to mimic the methanation conditions (Fig. 5b,d), the bands corresponding to b–CO_3 and HCOO remain at similar wavenumbers as during the CO_2 adsorption probing; however, the difference in intensity between them decreases. Furthermore, the methoxy bands increase and a new band appears at 1710 cm⁻¹ for both catalysts that can be attributed to the formation of formyl (CHO) groups [24].

To gain a deeper understanding of the reaction mechanism, we next conducted modulation-excitation phase-sensitive detection DRIFTS (ME–PSD–DRIFTS), allowing for a better signal-to-noise ratio plus distinguishing spectator and intermediate species. The modulated conditions applied in the experiments were a change in flowrate from A (CO_2 = 2.5 cm³ min⁻¹ and 10%H_2/N_2 = 100 cm³ min⁻¹) to B (CO_2 = 2.5 cm³

min⁻¹ and N_2 = 100 cm³ min⁻¹). Fig. 6 shows the phase-resolved spectra of the modulation excitation *in situ* DRIFTS studies conducted for **Ni/CeO₂** at 250, 300, and 350 °C. A comparison of Fig. 5 and Fig. 6 show that the data from the ME–PSD–DRIFTS experiments look quite different from those of the steady state experiments. In particular, three main differences can be identified: (i) the peak detected in the steady-state spectra at 1700 cm⁻¹ (Fig. 5b) is actually caused by a convolution of 2 peaks that are out-of-phase during modulation (Fig. 6); (ii) instead of 4 peaks observed in the steady-state spectra between 1700 and 1200 cm⁻¹ (Fig. 5b), the phase-resolved spectra show 7 peaks (Fig. 6), indicating the appearance of new groups not identified in the steady-state spectra, namely, p – CO_3 and carboxylate ($CO_2^{\delta-}$) groups (Table 2); and (iii) two from those 7 peaks are out-of-phase with the others (Fig. 6).

With regards to the aforementioned first difference, the band at 1700 cm⁻¹ is indicative of the formyl (CHO) group, while the band at 1760 cm⁻¹ is most likely related to bridged CO (br–CO) on Ni^0 sites [20, 24]. The appearance of br–CO on Ni^0 should be related to two reactions occurring simultaneously: it can be formed by direct dissociation of CO_2
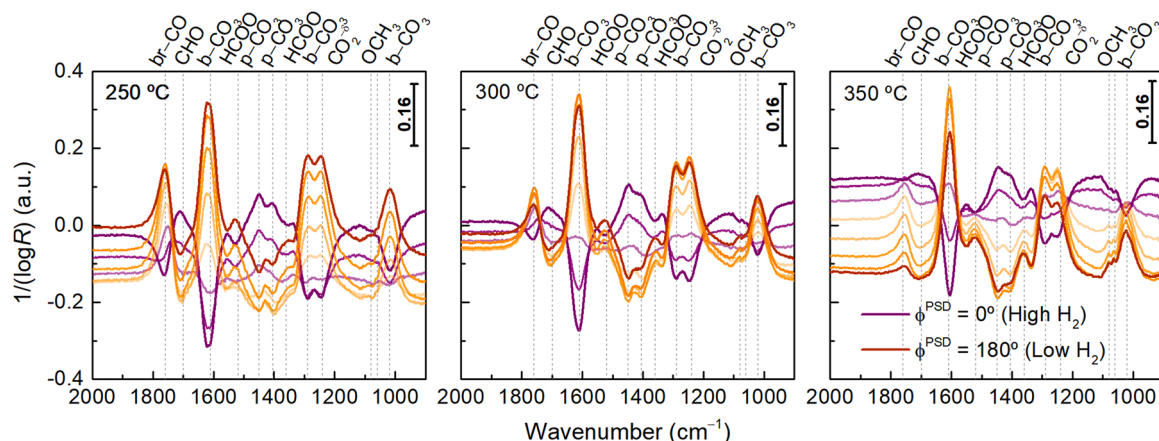
Fig. 6. Phase-resolved spectra of the modulation excitation *in situ* DRIFTS studies conducted for the Ni/CeO$_2$ catalyst at 250, 300 and 350 °C. Experimental conditions: $P = 1$ bar; flowrate A: $CO_2 = 2.5$ cm^3 min^{-1} and 10%H$_2$/N$_2 = 100$ cm^3 min^{-1}; flowrate B: $CO_2 = 2.5$ cm^3 min^{-1} and N$_2 = 100$ cm^3 min^{-1}; $m_{cat} = 15$ mg. The dashed lines indicate the positions of the peaks.

over Ni, and it can be a product of HCOO dissociation, since the presence of CO2$^{\delta-}$, b–CO$_3$, p–CO$_3$ and HCOO bands indicate that CO$_2$ should also be adsorbed and hydrogenated on CeO$_2$.

Furthermore, there is a possibility that br–CO can be hydrogenated to CHO in the presence of H$_2$, as previously reported [24]. This is a likely scenario since the respective bands are out of phase with each other, indicating that br–CO is hydrogenated to CHO on the surface of CeO$_2$ in the presence of H$_2$. A more detailed analysis of the phase delay φ (the time to reach maximum accumulation) for both br–CO and CHO species over **Ni/CeO$_2$** at 300 °C, show that they differ by 180° [φ(br–CO) = 108° and φ(CHO) = 288°]. This phase delay means that the CHO is formed at the same time as br–CO is consumed. Another possible scenario would be that this phase delay is dependent on that of the H$_2$, which would mean that H$_2$ favors the net formation of b–CO and disfavors the formation of CHO, leading to the maximum coverage of b–CO being observed mostly in phase with H$_2$, whereas CHO is mostly out of phase to H$_2$. However, since the phase delays are not close to 0° or 180°, which would be close to the value where H$_2$ is maximum and minimum, respectively, due to low residence time, the first option is more probable: br–CO should be hydrogenated to CHO in the presence of H$_2$. Notably, it is not possible to present the phase delay values for the remaining intermediates due to the accumulation of multiple maxima.

More detailed analysis of the differences between the steady-state and ME–PSD data reveal that while the bands from b–CO$_3$ appear at the same positions (Table 2) [10,26], the set of bands associated with HCOO in the steady-state spectra (Fig. 5b) are, in fact, a convolution of different species, namely, HCOO and p–CO$_3$ (Fig. 6, Table 2) [10]. Notably, the later p–CO$_3$ assignment could also be ascribed to mono-dentate carbonates (m–CO$_3$), but the low Δ_{as-s} suggests the presence of p–CO$_3$ rather than m–CO$_3$ [10]. In that case, p–CO$_3$ appearance is out-of-phase with b–CO$_3$ appearance, which indicate that the coordination of the carbonates may be changing from b–CO$_3$ to p–CO$_3$. Previously, this effect was explained as a change in carbonate adsorption configuration over CeO$_2$ as a consequence of its reduction state. Specifically, in the absence of H$_2$ ($\phi^{PSD} = 180°$), CeO$_2$ is partially oxidized, and when it is reduced in the presence of H$_2$ ($\phi^{PSD} = 0°$), the b–CO$_3$ reconfigures to either m–CO$_3$ or p–CO$_3$ [10].

Finally, only one peak was observed at 1270 cm^{-1} in the steady-state spectrum (Fig. 5b). After phase-sensitive detection analysis (PSD), two peaks are distinguished (Fig. 6): one from b–CO$_3$ and another one that we assign to CO$_2^{\delta-}$ (Table 2), typically forming when CO$_2$ is adsorbed on the surface of CeO$_2$ [10,24–26,43]. Finally, we assign the bands at $1080 - 1060$ cm^{-1} (Fig. 6) to methoxy (OCH$_3$) species [24,25], and the one at 1060 cm^{-1} corresponds to b–CO$_3$ (Table 2) [26].

When we compare the spectra at different temperatures (Fig. 6), we

observe that the bands remain at the same positions in all spectra, although their relative intensities varied. The change in intensity is particularly clear from the relative difference between the two peaks assigned to br–CO on Ni^0 and CHO, respectively. In contrast, the peaks from b–CO$_3$ and p–CO$_3$ remain intense, as they are known to be relatively stable [10].

Motivated by this detailed insight, we then proceeded to investigate the composite **Ni/ACR–CeO$_2$** catalyst by ME–PSD–DRIFTS. Due to the absorption of most of the IR radiation by the activated carbon, we observe a lower signal-to-noise ratio for **Ni/ACR–CeO$_2$** (Fig. 7) compared to **Ni/CeO$_2$** (Fig. 6). Nevertheless, we were still able to draw some conclusions from the phase-resolved spectra. First, the same species are detected in the ME–PSD–DRIFTS spectra of **Ni/ACR–CeO$_2$**, as in the case of **Ni/CeO$_2$**, moreover at nearly the same band positions (Figs. 6,7). However, three main differences were identified between methanation behaviors of these two catalysts: (i) in **Ni/ACR–CeO$_2$**, the relative intensity of br–CO band in comparison with CHO band (Fig. 7) is lower than in the case of **Ni/CeO$_2$** (Fig. 6); (ii) as the reaction temperature increases the presence of CO is not observed for **Ni/ACR–CeO$_2$** (Fig. 7); and (iii) the bands corresponding to p–CO$_3$ are significantly less pronounced for **Ni/ACR–CeO$_2$** (Fig. 7) than for **Ni/CeO$_2$** (Fig. 6). These differences show that, in sharp contrast to **Ni/CeO$_2$**, there is no direct transformation between br–CO and CHO over the **Ni/ACR–CeO$_2$** catalyst, which is further confirmed by the absence of CO at high temperatures (Fig. 7).

The full-range *in situ* ME–PSD–DRIFTS spectra may help to explain the general trends of the methanation over the synthesized catalysts and deviations between them. Fig. S10 shows that, with the **Ni/CeO$_2$** catalyst, the band corresponding to gaseous CH$_4$ at 3017 cm^{-1} is not present at 250 °C but it appears at 300 °C. Fig. S11 shows the same observations with the **Ni/ACR−CeO$_2$** catalyst. For both samples, the band corresponding to gaseous CO at 2200–2100 cm^{-1} starts to be apparent at 300 °C and is even more pronounced at 350 °C (Figs. S10, S11) [25]. For comparison, we also investigated the pure CeO$_2$ and composite ACR–CeO$_2$ supports without Ni being present and the obtained results are displayed in Figs. S12 and S13, respectively.

4. Discussion

It is well known that CeO$_2$-supported Ni catalysts have high activity and selectivity for CO$_2$ methanation at low temperatures, typically ≤ 400 °C. Most likely, these properties are related to the improved metal–support interactions between Ni and CeO$_2$ and a high surface coverage of CO$_2$, alternatively, they can be explained by the reducibility of CeO$_2$ [44].
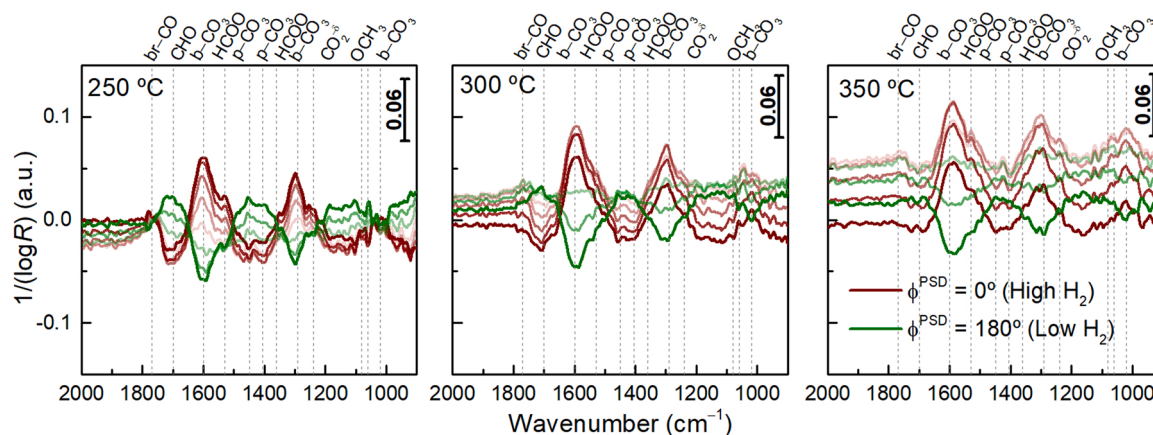
Fig. 7. Phase-resolved spectra of the modulation excitation *in situ* DRIFTS studies conducted for the Ni/ACR–CeO$_2$ catalyst at 250, 300 and 350 °C. Experimental conditions: P = 1 bar; flowrate A: CO$_2$ = 2.5 cm^3 min^{-1} and 10%H$_2$/N$_2$ = 100 cm^3 min^{-1}; flowrate B: CO$_2$ = 2.5 cm^3 min^{-1} and N$_2$ = 100 cm^3 min^{-1}; m_{cat} = 15 mg. The dashed lines indicate the positions of the peaks.

Based on our previous work [2], we hypothesized that an interesting approach to obtain high-performing methanation catalyst would be the preparation of Ni catalyst supported on composite supporting material consisting of reduced activated carbon and CeO$_2$.

Furthermore, we wanted to study whether such compositing would generate an active, selective, and stable methanation catalyst that operates at a temperature below 400 °C. Thus, we synthesized a set of 15 wt% Ni catalysts supported on ACR–CeO$_2$ with different ratios of ACR:CeO$_2$, as well as a 15 wt% Ni catalyst supported on pure CeO$_2$ (**Ni/CeO$_2$**) for reference. Fig. S1 shows that **Ni/ACR–CeO$_2$** with ACR:CeO$_2$ weight ratio of 50:50 afforded the best methanation performance. Besides improving the activity and selectivity compared to those for our previously reported **Ni/ACR**, the **Ni/ACR–CeO$_2$** catalyst achieved improved stability over long TOS at the respective optimal temperature. This improvement can be explained by the different interactions between the Ni and the pure ACR and ACR–CeO$_2$ composite and also by the fact that lowering the reaction temperature to 370 °C (cf. 450 °C) decreases the possibility of Ni deactivation over long TOS.

Significantly, although half of the supporting material in **Ni/ACR–CeO$_2$** is reduced activated carbon, we observed that the catalytic properties of the composite catalyst are comparable or even slightly better than those of **Ni/CeO$_2$** (Fig. 1). This result highlights that our compositing strategy is a useful tool for reducing the usage of the expensive rare-earth CeO$_2$ by replacing this oxide with a cost-effective carbon material. As explained in our previous work [2], the Lewis basic sites present on the ACR supporting material improve the Ni dispersion, and furthermore, its basicity is responsible for an improved CO$_2$ adsorption capacity over the catalyst, enabling CO$_2$ to be close to the Ni active sites.

The characterization of the samples allowed some property-performance relationships to be established. Even though the samples presented comparable catalytic performance, they are composed of materials with different textural properties. Furthermore, the Ni species on **Ni/CeO$_2$** exhibit a stronger interaction with pure CeO$_2$ support, compared to that in composite **Ni/ACR–CeO$_2$**, which can be a hypothesis for the fact that **Ni/ACR–CeO$_2$** presented slightly better activity at lower temperature. The reducibility of CeO$_2$ could also be a possible reason for slight differences in catalytic performance [44]; however, it is difficult to compare the reducibility of CeO$_2$ in CeO$_2$ and ACR−CeO$_2$ supports by H$_2$ −TPR analysis because ACR can undergo decomposition above 500 °C, which influences with the TPR profile of the sample above this temperature. The microscopy analysis demonstrated that in both samples, the particles exhibit Ni@NiO core-shell appearance.

XPS analysis revealed that both catalysts, **Ni/CeO$_2$** and **Ni/ACR–CeO$_2$**, exhibited two different Ni phases, corresponding to metallic Ni and NiO, with Ce 3d spectra also revealing the presence of mixed Ce phases in both samples. Interestingly, relative at% of Ce^{3+} is different in both samples, with the **Ni/ACR–CeO$_2$** catalyst exhibiting a higher value. It is known that the oxygen vacancies can be formed in the transformation process of Ce^{4+} into Ce^{3+}; thus, the amount of oxygen vacancies is usually proportional to the Ce^{3+} amount [34]. Therefore, we can hypothesize that **Ni/ACR–CeO$_2$** catalyst may contain a higher amount of oxygen vacancies, which are known to be important in the methanation reaction, than does **Ni/CeO$_2$**. This hypothesis cannot be directly supported by the analysis of the O 1s spectra because the O 1s spectra of **Ni/ACR–CeO$_2$** contain components from the organic phase of ACR, in addition to the components related to CeO$_2$ (Fig. S7) [31,33,35, 45].

After the stability experiment over a long TOS, the major modification was observed in **Ni/ACR–CeO$_2$**, in which the CeO$_2$ particles presented a needle-like shape. Most likely, the presence of steam, a subproduct of the reaction, leads to hydrothermal recrystallization of the initial CeO$_2$ nanoparticles into CeO$_2$ nanoneedles. This recrystallization is apparently templated by the presence of ACR, since carbon-free **Ni/CeO$_2$** did not exhibit the appearance of the CeO$_2$ needles after TOS testing (Fig. S8a). The carbon balance, that was close to zero, and the fact that our catalysts do not suffer deactivation over 90 h, indicate that carbon deposition should be minimal, if present at all, in these systems.

Our studies of CO$_2$ methanation over **Ni/CeO$_2$** and **Ni/ACR–CeO$_2$** have established that both catalysts demonstrated outstanding catalytic activity, selectivity, and stability in CO$_2$ methanation (Fig. 1). Notably, Ni catalysts supported on CeO$_2$ are among the materials exhibiting the highest methanation performance reported in the literature. To our gratification, the observed catalytic properties for our **Ni/CeO$_2$** and **Ni/ACR–CeO$_2$** catalysts compare favorably to the reported ones. Specifically, our catalysts achieved a maximum X_{CO2} of 86% and 87%, with $S_{CH4} \approx 100\%$ at 370 °C, while having a T_{50} of 280 °C; this T_{50} is similar or even lower from most of the reported in the literature for similar catalytic systems (Table S3). For example, Rui *et al.* [20] prepared two different CeO$_2$ supports that were used for the preparation of two Ni-based catalysts, which could achieve $X_{CO2} \approx 85\%$ with $S_{CH4} \approx 100\%$ at 275 °C ($T_{50} \approx 260$ °C) and 350 °C ($T_{50} \approx 280$ °C). In another interesting report, which compares two differently synthesized Ni on CeO$_2$ catalysts, Ye *et al.* [24] observed $X_{CO2} = 82.5\%$ and $S_{CH4} = 94.8\%$ at 250 °C with Ni/CeO$_2$–SGM catalyst (synthesized via sol-gel method), as well as $X_{CO2} = 69.8\%$ and $S_{CH4} = 84.8\%$, at 450 °C with Ni/CeO$_2$-IM (prepared by a simple impregnation method). They used conditions similar to those in the present study, albeit at a lower (10,000 cf. 60, 000 cm^3 g^{-1} h^{-1}) weight hourly space velocity (*WHSV*); the catalysts exhibited a T_{50} of ≈ 240 °C and ≈ 380 °C, respectively. In another study

with two differently synthesized CeO_2 supports, with and without a g–C_3N_4 template, Yu *et al.* [25] obtained two Ni-based catalysts exhibiting T_{50} of 305 °C and 330 °C, with maximum $X_{CO2} \approx 75\%$ and $S_{CH4} \approx 100\%$, at 350 °C and 400 °C, for the catalyst prepared with g–C_3N_4 template and without, respectively, also at a lower *WHSV* (10,000 cf. 60, 000 cm^3 g^{-1} h^{-1}). Cárdenas-Arenas *et al.* [26] prepared a Ni/CeO_2 catalyst that reached $\approx 85\%$ X_{CO2} with $\approx 100\%$ S_{CH4} at 375 °C, with T_{50} of ≈ 280 °C.

The mechanism of the CO_2 methanation over Ni/CeO_2 catalysts has been a subject of intensive research. Zhang *et al.* [19] investigated the reaction mechanism on Ni/CeO_2 by first-principles calculations and concluded that the reaction on this catalyst follows the CO pathway through reverse water gas shift, rather than the formate (HCOO) formation or direct C–O bond cleavage pathways. Based on *in situ* DRIFTS study, Lee et al. [23] compared the mechanism of CO_2 methanation for Ni-based catalysts supported on different materials. They concluded that the Ni/CeO_2 catalyst, dissociates CO_2 into CO, which then participates in the CO_2 methanation reaction at high temperature. In another study with a Ni/CeO_2 catalyst synthesized by the sol-gel method, Ye *et al.* [24] suggested that the reaction occurred through a formate (HCOO) pathway with formyl (CHO) intermediate. Furthermore, the authors suggested that the good performance of the catalysts was related to the effective dissociation of H_2 by Ni and the strong adsorption/activation of CO_2 by CeO_2 support. Based on a DRIFTS study, Rui *et al.* [20] determined that the reaction proceeded through the CO pathway over Ni/CeO_2 catalyst, namely, by direct C–O bond cleavage via reverse water gas shift reaction followed by the methanation of the resultant CO.

Although some studies have indicated that CO_2 methanation over Ni/CeO_2 proceeds through the CO pathway [19,20,23], our results show that the methanation over our **Ni/CeO₂** follows a combination of CO pathway and the formate (HCOO) pathway, where CO forms through HCOO dissociation.

For **Ni/CeO₂**, we observed from steady-state *in situ* DRIFTs experiments (Fig. 5) that the CO_2 adsorption on the catalyst resulted in the formation of b–CO_3 and HCOO. When H_2 was added to the gas flow generating methanation conditions, another band attributed to CHO appeared, indicating that CHO is an important intermediate for the methanation over **Ni/CeO₂** catalyst.

The ME–PSD–DRIFT methodology improved the signal-to-noise ratio and allowed us to distinguish between the spectator and intermediate species. Now for **Ni/CeO₂**, it was possible to observe that the peak attributed to CHO in the steady-state *in situ* DRIFTS was in fact composed of two peaks out-of-phase with each other, namely, br–CO on Ni^0 and CHO [20,24].

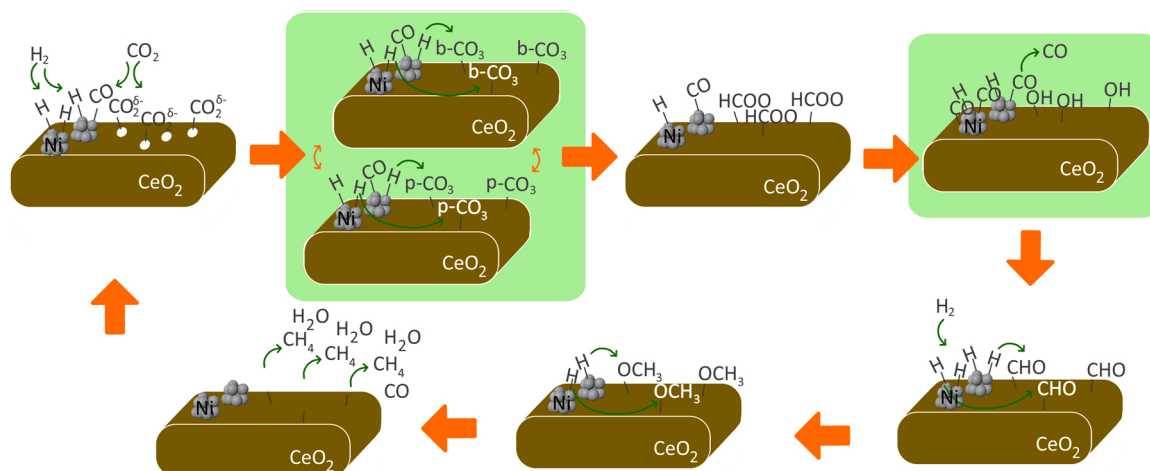Based on the collected experimental in situ ME–PSD–DRIFTS evidence (Fig. 6, S10, S12 and Table 2), Scheme 1 outlines the envisioned mechanism of the CO_2 methanation over synthesized **Ni/CeO₂**. There are two possibilities for the formation of br–CO on Ni^0: by direct dissociation of CO_2 over Ni, or dissociation of HCOO. In the second case, specifically, CO_2 is adsorbed on the CeO_2 surface as $CO_2^{\delta-}$, which then forms b–CO_3/p–CO_3 species [43]. These species are then hydrogenated by the hydrogen dissociated over Ni^0 to form HCOO, which is further dissociated forming br–CO on Ni^0. Next, the br–CO is firstly hydrogenated to CHO over the CeO_2 [24] and then to OCH_3, as observed in the respective in situ ME–PSD–DRIFTS spectra (Fig. 6, Table 2). It is difficult to access the phase delay of the methoxy species, due to a small signal being observed, but according to the literature, the presence of OCH_3 indicate that CHO should be hydrogenated to this species. Eventually, the as-formed OCH_3 is sequentially hydrogenated to CH_4 and released as the end-product.

There is an alternative pathway in which br–CO could be only involved in CO formation and not in the formation of the desired CH_4, and, accordingly, CHO would be formed through direct dissociation of HCOO. However, the fact that b–CO and CHO bands are 180° out-of-phase with each other (Fig. 6) strongly suggests that their transformation is directly correlated, which rules out this pathway.

When comparing the carbon-containing **Ni/ACR–CeO₂** to the carbon-free **Ni/CeO₂**, our characterization data indicate that the catalysts are quite different. **Ni/ACR–CeO₂** has a significantly higher surface area, porosity, and metallic Ni surface area, with smaller Ni nanoparticles size in comparison with **Ni/CeO₂**. At the same time, **Ni/CeO₂** is expected to have stronger metal–support interactions. The observation of similar methanation properties for such different catalysts leads to the hypothesis that the CO_2 methanation over **Ni/ACR–CeO₂** and **Ni/CeO₂** might proceed through different mechanisms.

The presence of CHO and especially the br–CO intermediates are less pronounced in **Ni/ACR–CeO₂** (Fig. 7), while the relative intensity of the HCOO, compared to the other species, appears to be higher (Fig. 7) than in the case of **Ni/CeO₂** (Fig. 6). Additionally, at higher temperature of 350 °C, the presence of the band from br–CO is not observed (Fig. 7). This could be explained by the fact that the consumption rate of CO on this catalyst is more favored by high temperatures than the formation rate, leading to less accumulation of this intermediate. However, if we consider that CO is hydrogenated to CHO, the instantaneous reaction (with lack of CO accumulation) would lead to a higher accumulation of CHO, if CHO is not hydrogenated at the same rate as CO, which is not observed. Therefore, the disappearance of the band from br–CO at high temperatures is related to desorption, instead of hydrogenation to CHO.

Thus, the data indicate that the br–CO does not play a significant role in the reaction pathway but may be related to the formation of the CO

Scheme 1. Proposed mechanism for the CO_2 methanation over Ni/CeO_2 catalyst, displaying the formation/transformation of the reaction intermediates as elucidated by *in situ* ME–PSD–DRIFTS. The green boxes mark the differences in the mechanism between the two samples (Scheme 1 vs. Scheme 2).

byproduct (Scheme 2 (b)).

Regarding Ni catalysts supported on carbon materials, Hu *et al.* [17] concluded that the methanation over Ni catalyst supported on graphene aerogel followed the formate pathway, with carbonate intermediates being present, i.e., without the formation of CO. Consistently with this report, the CO_2 methanation over our carbon-containing **Ni/ACR–CeO₂** catalyst proceeds through the formate pathway, which is depicted on Scheme 2 (a). The methanation starts with the adsorption of CO_2 as $CO_2^{\delta-}$, followed by the formation of b–CO_3/p–CO_3 species [43]. Those are then hydrogenated to HCOO, similarly to what we observed for the carbon-free **Ni/CeO₂**. At the same time, in sharp contrast to **Ni/CeO₂**, br–CO was not detected for **Ni/ACR–CeO₂** at higher temperatures (350 °C). This fact indicates the significant difference between methanation over **Ni/CeO₂** and **Ni/ACR–CeO₂**, wherein over the composite catalyst, the formate (HCOO) is directly dissociated to formyl (CHO) [46], then following the same pathway as over the **Ni/CeO₂**. In particular, CHO is further hydrogenated to methoxy and finally to methane end product.

With regards to the proposed mechanisms (Schemes 1, 2), it is important to emphasize that some of the H_2 can be partially dissociated on the CeO_2 surface (i.e., not only on the Ni^0). This is suggested by *in situ* ME–PSD–DRIFTS of pure CeO_2 and composite ACR–CeO_2 supporting materials, revealing the presence of partially hydrogenated HCOO and OCH_3 species (Figs. S12, S13).

Interestingly, our detailed electron microscopy investigation of the microstructural changes, together with the XPS analysis, within the catalysts after 90 h of time-on-stream testing evidences that even though the catalysts did not lose their catalytic performance over 90 h (Fig. 1c, d), their fine microstructure and chemical composition were indeed affected.

The analysis of the Ni $2p_{3/2}$ and Ce 3d spectra of the fresh and TOS tested **Ni/CeO₂** and **Ni/ACR–CeO₂** revealed alterations in the Ni^0 content and the Ce^{3+}/Ce^{4+} ratios. The Ni^0 relative at% increase in **Ni/ACR–CeO₂ ₜₒₛ** indicating that the Ni nanoparticles likely undergo a further reduction under the reductive conditions of the CO_2 methanation reaction, probably due to the higher reducibility and weaker metal-support interactions in this sample (Fig. S4). On the contrary, an increase in the Ni^0 relative at% is observed in **Ni/CeO₂**. Regarding the CeO_2 support, Ce 3d spectra indicate that the relative at% of Ce^{3+}, and

consequently the amount of oxygen vacancies remain similar in the **Ni/ACR–CeO₂ ₜₒₛ**, while, in contrast, increasing under reaction conditions in **Ni/CeO₂**.

The microstructural changes are mostly reflected by the preservation of the shell around Ni particles in both TOS-tested **Ni/CeO₂** and **Ni/ACR-CeO₂** materials (Fig. 4,S8). The catalytic functions of the observed NiO shells are not well understood and our future work underpinning the role of the shell in the CO_2 methanation over high-performing Ni catalysts is ongoing.
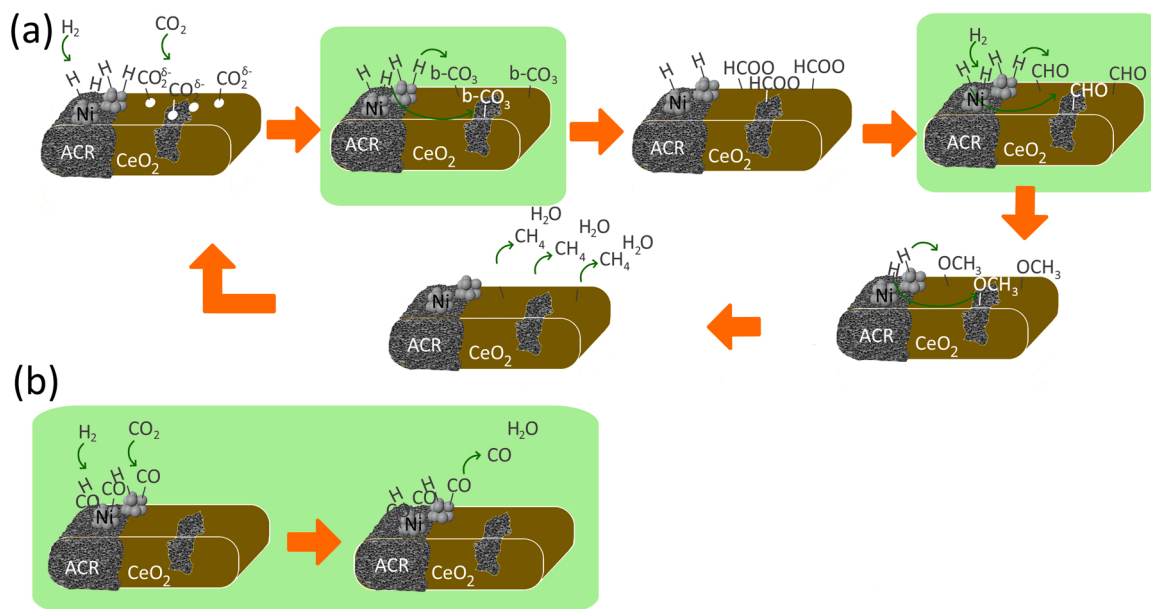
5. Conclusions

A set of Ni catalysts deposited either on pure CeO_2 or composite carbon–CeO_2 supporting materials have been synthesized and characterized. CO_2 methanation with excellent conversion, selectivity and stability at favorably low reaction temperature was achieved using the as-synthesized **Ni/CeO₂** and **Ni/ACR–CeO₂** catalysts.

Our work demonstrated that compositing carbon with CeO_2 within the supporting material afforded an effective reduction in the usage of the expensive rare-earth CeO_2 while providing access to not only a cost-effective but also a high-performing methanation catalyst operating at low temperature. The mechanism of the CO_2 methanation over the newly synthesized catalysts was investigated by means of in situ spectroscopy, using the emerging ME−PSD−DRIFTS technique. The collected insights uncovered that the methanation over **Ni/CeO₂** proceeded via a combination of the CO and formate pathways, while in **Ni/ACR–CeO₂** it proceeded exclusively via the formate pathway. The main underlying mechanistic difference between the catalysts is that, during methanation over carbon-free **Ni/CeO₂**, the reaction is mediated by CO from both CO_2 and formate dissociation, while carbon-containing **Ni/ACR–CeO₂** catalyst is producing CH_4 without intermediate CO formation. Overall, these results illustrated that even partial modification of the supporting material for Ni methanation catalysts can influence the reaction mechanism.

CRediT authorship contribution Statement

Liliana P.L. Gonçalves: Conceptualization, Methodology, Formal analysis, Investigation, Writing – original draft. **Jerrik Mielby:**

Scheme 2. Proposed mechanism for the CO_2 methanation over Ni/ARC–CeO₂ catalyst, displaying the formation/transformation of the reaction intermediates as elucidated by *in situ* ME–PSD–DRIFTS. (a) illustrates the mechanism of CH_4 formation while (b) depicts the mechanism of CO formation. The green boxes mark the differences in the mechanism between the two samples (Scheme 1 vs. Scheme 2).

Conceptualization, Methodology, Writing – review & editing. **O. Salomé G.P. Soares:** Methodology, Writing – review & editing, Supervision. **Juliana P.S. Sousa:** Writing – review & editing, Supervision. **Dmitri Y. Petrovykh:** Writing – review & editing. **Oleg I. Lebedev:** Writing – review & editing, Funding acquisition. **M. Fernando R. Pereira:** Writing – review & editing, Supervision, Funding acquisition. **Søren Kegnæs:** Conceptualization, Writing – review & editing, Funding acquisition. **Yury V. Kolen'ko:** Conceptualization, Writing – original draft, Supervision, Funding acquisition.

Declaration of Competing Interest

The authors declare that they have no known competing financial interests or personal relationships that could have appeared to influence the work reported in this paper.

Acknowledgments

Appendix A. Supporting information

Supplementary data associated with this article can be found in the online version at doi:10.1016/j.apcatb.2022.121376.

References

[1] J. Ashok, S. Pati, P. Hongmanorom, Z. Tianxi, C. Junmei, S. Kawi, A review of recent catalyst advances in CO_2 methanation processes, Catal. Today 356 (2020) 471–489, https://doi.org/10.1016/j.cattod.2020.07.023.

[2] L.P.L. Gonçalves, J.P.S. Sousa, O.S.G.P. Soares, O. Bondarchuk, O.I. Lebedev, Y. V. Kolen'ko, M.F.R. Pereira, The role of surface properties in CO_2 methanation over carbon-supported Ni catalysts and their promotion by Fe, Catal. Sci. Technol. 10 (2020) 7217, https://doi.org/10.1039/D0CY01254H.

[3] B. Miao, S.S.K. Ma, X. Wang, H. Su, S.H. Chan, Catalysis mechanisms of CO_2 and CO methanation, Catal. Sci. Technol. 6 (2016) 4048–4058, https://doi.org/10.1039/C6CY00478D.

[4] F. Goodarzi, L. Kang, F.R. Wang, F. Joensen, S. Kegnæs, J. Mielby, Methanation of carbon dioxide over zeolite-encapsulated nickel nanoparticles, ChemCatChem 10 (2018) 1566–1570, https://doi.org/10.1002/cctc.201701946.

[5] L.P.L. Gonçalves, A. Serov, G. McCool, M. Dicome, J.P.S. Sousa, O.S.G.P. Soares, O. Bondarchuk, D.Y. Petrovykh, O.I. Lebedev, M.F.R. Pereira, Y. Kolen'ko, New opportunity for carbon-supported Ni-based electrocatalysts: gas-phase CO_2 methanation, ChemCatChem 13 (2021) 1–11, https://doi.org/10.1002/cctc.202101284.

[6] Z. Zhang, Y. Tian, L. Zhang, S. Hu, J. Xiang, Impacts of nickel loading on properties, catalytic behaviors of Ni/γAl$_2$O$_3$ catalysts and the reaction intermediates formed in methanation of CO_2, Int. J. Hydrog. Energy 44 (2019) 9291–9306, https://doi.org/10.1016/j.ijhydene.2019.02.129.

[7] T.A. Le, M.S. Kim, S.H. Lee, E.D. Park, CO and CO_2 methanation over supported cobalt catalysts, Top. Catal. 60 (2017) 714–720, https://doi.org/10.1007/s11244-017-0788-y.

[8] G. Zhou, T. Wu, H. Xie, X. Zheng, Effects of structure on the carbon dioxide methanation performance of Co-based catalysts, Int. J. Hydrog. Energy 38 (2013) 10012–10018, https://doi.org/10.1016/j.ijhydene.2013.05.130.

[9] D.L. Williamson, M.D. Jones, D. Mattia, Highly selective, iron-driven CO_2 methanation, Energy Technol. 7 (2019) 294–306, https://doi.org/10.1002/ente.201800923.

[10] F. Hemmingsson, A. Schaefer, M. Skoglundh, P.A. Carlsson, CO_2 methanation over Rh/CeO$_2$ studied with infrared modulation excitation spectroscopy and phase sensitive detection, Catalysts 10 (2020) 601, https://doi.org/10.3390/catal10060601.

[11] H. Chen, F. Goodarzi, Y. Mu, S. Chansai, J.J. Mielby, B. Mao, T. Sooknoi, C. Hardacre, S. Kegnæs, X. Fan, Effect of metal dispersion and support structure of Ni/silicalite-1 catalysts on non-thermal plasma (NTP) activated CO_2

[12] hydrogenation, Appl. Catal. B Environ. 272 (2020) 119013, https://doi.org/10.1016/j.apcatb.2020.119013.

[12] K.H. Rasmussen, F. Goodarzi, D.B. Christensen, J. Mielby, S. Kegnæs, Stabilization of metal nanoparticle catalysts via encapsulation in mesoporous zeolites by steam-assisted recrystallization, ACS Appl. Nano Mater. 2 (2019) 8083–8091, https://doi.org/10.1021/acsanm.9b02205.

[13] I. Champon, A. Bengaouer, A. Chaise, S. Thomas, A.C. Roger, Carbon dioxide methanation kinetic model on a commercial Ni/Al$_2$O$_3$ catalyst, J. CO2 Util. 34 (2019) 256–265, https://doi.org/10.1016/j.jcou.2019.05.030.

[14] G. Garbarino, P. Riani, L. Magistri, G. Busca, A study of the methanation of carbon dioxide on Ni/Al$_2$O$_3$ catalysts at atmospheric pressure, Int. J. Hydrog. Energy 39 (2014) 11557–11565, https://doi.org/10.1016/j.ijhydene.2014.05.111.

[15] G.M. Shashidhara, M. Ravindram, A kinetic study of the methanation of CO_2 over Ni-Al$_2$O$_3$ catalyst, React. Kinet. Catal. Lett. 37 (1988) 451–456.

[16] W. Wang, C. Duong-Viet, H. Ba, W. Baaziz, G. Tuci, S. Caporali, L. Nguyen-Dinh, O. Ersen, G. Giambastiani, C. Pham-Huu, Nickel nanoparticles decorated nitrogen-doped carbon nanotubes (Ni/N-CNT); a robust catalyst for the efficient and selective CO_2 methanation, ACS Appl. Energy Mater. 2 (2019) 1111–1120, https://doi.org/10.1021/acsaem.8b01681.

[17] F. Hu, X. Chen, Z. Tu, Z.-H. Lu, G. Feng, R. Zhang, Graphene aerogel supported Ni for CO2 hydrogenation to methane, Ind. Eng. Chem. Res. 60 (2021) 12235–12243, https://doi.org/10.1021/acs.iecr.1c01953.

[18] J.L. Figueiredo, M.F.R. Pereira, M.M.A. Freitas, J.J.M. Órfão, Characterization of active sites on carbon catalysts, Ind. Eng. Chem. Res. 46 (2007) 4110–4115, https://doi.org/10.1021/ie061071v.

[19] J. Zhang, Y. Yang, J. Liu, B. Xiong, Mechanistic understanding of CO_2 hydrogenation to methane over Ni/CeO$_2$ catalyst, Appl. Surf. Sci. 558 (2021), 149866, https://doi.org/10.1016/j.apsusc.2021.149866.

[20] N. Rui, X. Zhang, F. Zhang, Z. Liu, X. Cao, Z. Xie, R. Zou, S.D. Senanayake, Y. Yang, J.A. Rodriguez, C.J. Liu, Highly active Ni/CeO$_2$ catalyst for CO_2 methanation: preparation and characterization, Appl. Catal. B Environ. 282 (2021), 119581, https://doi.org/10.1016/j.apcatb.2020.119581.

[21] P. Hongmanorom, J. Ashok, P. Chirawatkul, S. Kawi, Interfacial synergistic catalysis over Ni nanoparticles encapsulated in mesoporous ceria for CO_2 methanation, Appl. Catal. B Environ. 297 (2021) 120454, https://doi.org/10.1016/j.apcatb.2021.120454.

[22] S. Tada, T. Shimizu, H. Kameyama, T. Haneda, R. Kikuchi, Ni/CeO$_2$ catalysts with high CO_2 methanation activity and high CH$_4$ selectivity at low temperatures, Int. J. Hydrog. Energy 37 (2012) 5527–5531, https://doi.org/10.1016/j.ijhydene.2011.12.122.

[23] Y.H. Lee, J.Y. Ahn, D.D. Nguyen, S.W. Chang, S.S. Kim, S.M. Lee, Role of oxide support in Ni based catalysts for CO_2 methanation, RSC Adv. 11 (2021) 17648–17657, https://doi.org/10.1039/d1ra02327f.

[24] R.P. Ye, Q. Li, W. Gong, T. Wang, J.J. Razink, L. Lin, Y.Y. Qin, Z. Zhou, H. Adidharma, J. Tang, A.G. Russell, M. Fan, Y.G. Yao, High-performance of nanostructured Ni/CeO$_2$ catalyst on CO_2 methanation, Appl. Catal. B Environ. 268 (2020), 118474, https://doi.org/10.1016/j.apcatb.2019.118474.

[25] Y. Yu, Y.M. Chan, Z. Bian, F. Song, J. Wang, Q. Zhong, S. Kawi, Enhanced performance and selectivity of CO_2 methanation over g-C$_3$N$_4$ assisted synthesis of Ni–CeO$_2$ catalyst: kinetics and DRIFTS studies, Int. J. Hydrog. Energy 43 (2018) 15191–15204, https://doi.org/10.1016/j.ijhydene.2018.06.090.

[26] A. Cárdenas-Arenas, A. Quindimil, A. Davó-Quiñonero, E. Bailón-García, D. Lozano-Castelló, U. De-La-Torre, B. Pereda-Ayo, J.A. González-Marcos, J. R. González-Velasco, A. Bueno-López, Isotopic and in situ DRIFTS study of the CO_2 methanation mechanism using Ni/CeO$_2$ and Ni/Al$_2$O$_3$ catalysts, Appl. Catal. B Environ. 265 (2020), 118538, https://doi.org/10.1016/j.apcatb.2019.118538.

[27] P.C.C. Faria, J.J.M. Órfão, M.F.R. Pereira, A novel ceria – activated carbon composite for the catalytic ozonation of carboxylic acids, Catal. Commun. 9 (2008) 2121–2126, https://doi.org/10.1016/j.catcom.2008.04.009.

[28] B. Owens-Baird, J. Xu, D.Y. Petrovykh, O. Bondarchuk, Y. Ziouani, N. González-Ballesteros, P. Yox, F.M. Sapountzi, H. Niemantsverdriet, Y.V. Kolen'ko, K. Kovnir, NiP$_2$: a story of two divergent polymorphic multifunctional materials, Chem. Mater. 31 (2019) 3407–3418, https://doi.org/10.1021/acs.chemmater.9b00565.

[29] M.C. Biesinger, B.P. Payne, L.W.M. Lau, A. Gerson, R.S.C. Smart, X-ray photoelectron spectroscopic chemical state quantification of mixed nickel metal, oxide and hydroxide systems, Surf. Interface Anal. 41 (2009) 324–332, https://doi.org/10.1002/sia.3026.

[30] B. Owens-Baird, J.P.S. Sousa, Y. Ziouani, D.Y. Petrovykh, N.A. Zarkevich, D. D. Johnson, Y.V. Kolen'ko, K. Kovnir, Crystallographic facet selective HER catalysis: exemplified in FeP and NiP$_2$ single crystals, Chem. Sci. 11 (2020) 5007–5016, https://doi.org/10.1039/D0SC00676A.

[31] E. Bêche, P. Charvin, D. Perarnau, S. Abanades, G. Flamant, Ce 3d XPS investigation of cerium oxides and mixed cerium oxide (Ce$_x$Ti$_y$O$_z$), Surf. Interface Anal. 40 (2008) 264–267, https://doi.org/10.1002/sia.2686.

[32] F. Zhang, P. Wang, J. Koberstein, S. Khalid, S.W. Chan, Cerium oxidation state in ceria nanoparticles studied with X-ray photoelectron spectroscopy and absorption near edge spectroscopy, Surf. Sci. 563 (2004) 74–82, https://doi.org/10.1016/j.susc.2004.05.138.

[33] D.R. Mullins, S.H. Overbury, D.R. Huntley, Electron spectroscopy of single crystal and polycrystalline cerium oxide surfaces, Surf. Sci. 409 (1998) 307–319, https://doi.org/10.1016/S0039-6028(98)00257-X.

[34] M. Nolan, J.E. Fearon, G.W. Watson, Oxygen vacancy formation and migration in ceria, Solid State Ion. 177 (2006) 3069–3074, https://doi.org/10.1016/j.ssi.2006.07.045.

[35] J.L. Figueiredo, M.F.R. Pereira, The role of surface chemistry in catalysis with carbons, Catal. Today 150 (2010) 2–7, https://doi.org/10.1016/j.cattod.2009.04.010.

[36] L.P.L. Gonçalves, D.B. Christensen, M. Meledina, L.M. Salonen, D.Y. Petrovykh, E. Carbó-Argibay, J.P.S. Sousa, O.S.G.P. Soares, M.F.R. Pereira, S. Kegnæs, Y. V. Kolen'Ko, Selective formic acid dehydrogenation at low temperature over a RuO$_2$/COF pre-catalyst synthesized on the gram scale, Catal. Sci. Technol. 10 (2020) 1991–1995, https://doi.org/10.1039/d0cy00145g.

[37] P.D. Srinivasan, B.S. Patil, H. Zhu, J.J. Bravo-Suárez, Application of modulation excitation-phase sensitive detection-DRIFTS for: in situ /operando characterization of heterogeneous catalysts, React. Chem. Eng. 4 (2019) 862–883, https://doi.org/10.1039/c9re00011a.

[38] A. Urakawa, T. Bürgi, A. Baiker, Sensitivity enhancement and dynamic behavior analysis by modulation excitation spectroscopy: principle and application in heterogeneous catalysis, Chem. Eng. Sci. 63 (2009) 4902–4909, https://doi.org/10.1016/j.ces.2007.06.009.

[39] A. Aguirre, S.E. Collins, Selective detection of reaction intermediates using concentration- modulation excitation DRIFT spectroscopy, Catal. Today 205 (2013) 34–40, https://doi.org/10.1016/j.cattod.2012.08.020.

[40] D. Baurecht, U.P. Fringeli, Quantitative modulated excitation Fourier transform infrared spectroscopy, Rev. Sci. Instrum. 72 (2001) 3782–3792, https://doi.org/10.1063/1.1400152.

[41] P.D. Srinivasan, K. Khivantsev, J.M.M. Tengco, H. Zhu, J.J. Bravo-Suárez, Enhanced ethanol dehydration on γ-Al$_2$O$_3$ supported cobalt catalyst, J. Catal. 373 (2019) 276–296, https://doi.org/10.1016/j.jcat.2019.03.024.

[42] S.M. Fehr, I. Krossing, Spectroscopic signatures of pressurized carbon dioxide in diffuse reflectance infrared spectroscopy of heterogeneous catalysts, ChemCatChem 12 (2020) 2622–2629, https://doi.org/10.1002/cctc.201902038.

[43] Y. Yu, Z. Bian, Z. Wang, J. Wang, W. Tan, Q. Zhong, S. Kawi, CO$_2$ methanation on Ni-Ce$_{0.8}$ M$_{0.2}$ O$_2$ (M=Zr, Sn or Ti) catalyst: suppression of CO via formation of bridging carbonyls on nickel, Catal. Today 2 (2020), https://doi.org/10.1016/j.cattod.2020.07.049. ⟨https://doi.org/10.1016/j.cattod.2020.07.049⟩.

[44] R. Tang, N. Ullah, Y. Hui, X. Li, Z. Li, Enhanced CO$_2$ methanation activity over Ni/CeO$_2$ catalyst by one-pot method, Mol. Catal. 508 (2021), 111602, https://doi.org/10.1016/j.mcat.2021.111602.

[45] X. Liao, Y. Zhang, M. Hill, X. Xia, Y. Zhao, Z. Jiang, Highly efficient Ni/CeO2 catalyst for the liquid phase hydrogenation of maleic anhydride, Appl. Catal. A Gen. 488 (2014) 256–264, https://doi.org/10.1016/j.apcata.2014.09.042.

[46] H.L. Huynh, J. Zhu, G. Zhang, Y. Shen, W.M. Tucho, Y. Ding, Z. Yu, Promoting effect of Fe on supported Ni catalysts in CO$_2$ methanation by in situ DRIFTS and DFT study, J. Catal. 392 (2020) 266–277, https://doi.org/10.1016/j.jcat.2020.10.018.